Performance of High-Power Gas-Flow Spark Gaps

John M. Kuhlman* and G. Marshall Molen†
Old Dominion University, Norfolk, Virginia

Results of an experimental investigation of the performance of repetitively pulsed gas-flow spark gaps are presented. Interelectrode gas-flow velocity and turbulence levels have been documented using pitot and hot-wire probes while transient arc debris behavior has been studied using schlieren optical techniques. Typical electrical recovery curves are presented at various gas velocities. Analysis of the recovery, flow, and optical diagnostic data has led to the development of a simple model for the recovery of a spark gap with gas flow.

Introduction

SPARK gaps have long been utilized as closing switches in a wide variety of pulsed power applications. One key limitation to high-pressure spark gap performance is the relatively low rate at which a spark gap may be repetitively switched. One means by which achievable repetition rates may be greatly increased is the use of gas flow between the electrodes to remove arc debris and heated gas from the previous arc before application of each subsequent pulse.

Since spark gaps have often been developed by users to meet specific applications, there have been relatively few controlled studies of the variation of spark gap performance with gas-flow parameters. Previous studies of gas-flow effects on spark gap performance have been surveyed by Kuhlman,[1] while considerations for future work are discussed by Molen and Carper.[2] The present paper describes typical results of an investigation into the physical processes affecting, and limiting, the performance of high-pressure, gas-flow spark gaps operating in the voltage range 100-250 kV, with peak currents of 50 kA, and a pulse width of 70 ns.

Measurements of switch performance and associated physical phenomena presented herein include: interelectrode mean and fluctuation velocity profiles, optical flow diagnostics, and electrical recovery of the spark gap for various gas species, velocities, pressures, and electrode spacings for a single, two-dimensional electrode geometry. A fast image converter camera (ICC) has been used in conjunction with a pulsed xenon flash lamp and schlieren optical system to record the transient shock due to the arc, as well as the expansion, mixing, and convection of the arc-generated heated gas column. The same ICC has also been used to record visible arc luminosity. Such schlieren and visible luminosity recordings have given valuable physical insight into the recovery process with gas flow.

Spark Gap Test Facility

The pulsed power system developed for this investigation, as described in Ref. 3 and shown in Fig. 1, supplies bursts of two identical voltage pulses to the spark gap, which are separated by a variable interpulse spacing that is as small as 100 μs. The peak voltage may be varied from 30 to 250 kV, and each voltage pulse has a rise time of about 10 μs. Gas flow is supplied to the spark gap under controlled conditions using either of two wind tunnels that have been developed for the study. A low-speed, closed-circuit, high-pressure tunnel[4] allows studies to be conducted at high pressure with various gas mixtures while a high-speed blowdown tunnel permits investigation of super and transonic speeds in air. This supersonic tunnel is of the asymmetrical, sliding nozzle block design described in Ref. 5 and will not be described further in the present paper since results from this tunnel are likewise not presented.

A schematic of the low-speed tunnel is shown in Fig. 2. The spark gap mounts inside the test chamber with the electrode axis concentric with the water-filled blumlein that supplies the voltage pulses to the switch. Gas flow is perpendicular to the electrode axis while flow visualization is possible through optical view ports in the test chamber. The gas flow is generated by a shaft-driven fan using a four-speed induction motor and cogged-belt overdrive. Low turbulence levels are achieved by use of a honeycomb flow straightener and screens upstream of the 13:1 area ratio nozzle placed just before the spark gap test section. The tunnel pressure vessel has a design pressure of 1.6 MPa (220 psig). One unique design feature of this tunnel is the use of standard aluminum pipe and fittings to form the pressure vessel, with nozzles and diffusers made from plastic or aluminum sheet metal, inserted into the pressure vessel. Secondly, the drive fan used is from a commercially available wind-tunnel propulsion simulator. These approaches simplified tunnel design and reduced cost. Further description of the tunnel design procedure and tunnel performance is given in Ref. 4.

Spark gap electrodes of various two-dimensional geometries are mounted in an epoxy cast insulator housing (Fig. 3) located inside the test chamber, fitted with a flow channel at a right angle to the electrode axis; the switch attaches to either of the two wind tunnels by smoothly contoured flow channel inserts placed inside the test chamber. Optical flow visualization is possible along a direction perpendicular to the electrode and flow axes through windows in the sides of the switch housing. The electrode gap spacing is adjustable so as to investigate a range of operating voltages. Also shown in Fig. 3 is one of the electrode geometries studied, termed the nipple-wing electrode pair, as well as examples of the types of flow diagnostic probes utilized. Either pitot or hot-wire probes may be traversed horizontally as shown in Fig. 3, or vertically between the electrode gap region using a specially designed flow diagnostic chamber and switch housing.

Velocity Survey Results

Horizontal traverses of the mean velocity and relative fluctuation profiles obtained using a pitot probe are shown in Fig. 4 at a location midway between the electrodes. The nipple-wing electrodes were separated a distance of $d=0.87$ cm in the low-speed tunnel at a pressure of 1 atm in N_2. Mean velocity is quite uniform at all tunnel speeds, while low-frequency velocity fluctuations sensed by the pitot probe are on the order of 0.5% of the mean velocity. Similar results are seen at pressures of 441-741 kPa (50-90 psig).

Received Nov. 20, 1984; presented as Paper 85-0134 at the AIAA 23rd Aerospace Sciences Meeting, Reno, NV, Jan. 14-17, 1985; revision submitted Aug. 30, 1985.

*Associate Professor, Department of Mechanical Engineering and Mechanics. Member AIAA.

†Professor, Department of Electrical Engineering.

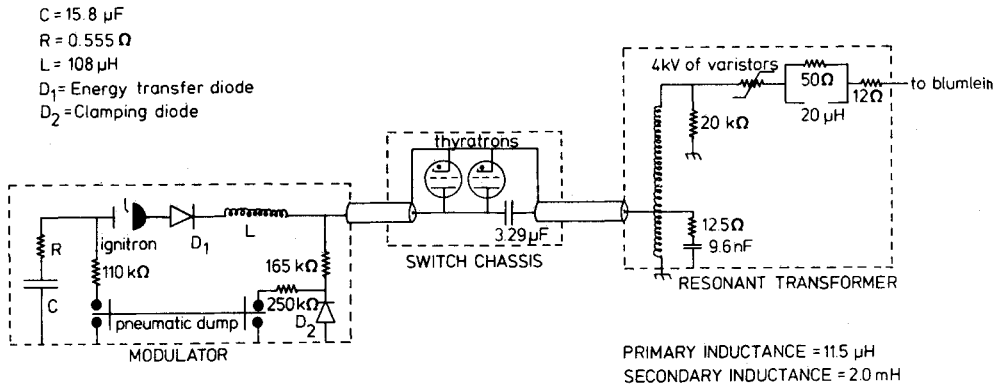

Fig. 1 Basic diagram of the pulsed power circuit.

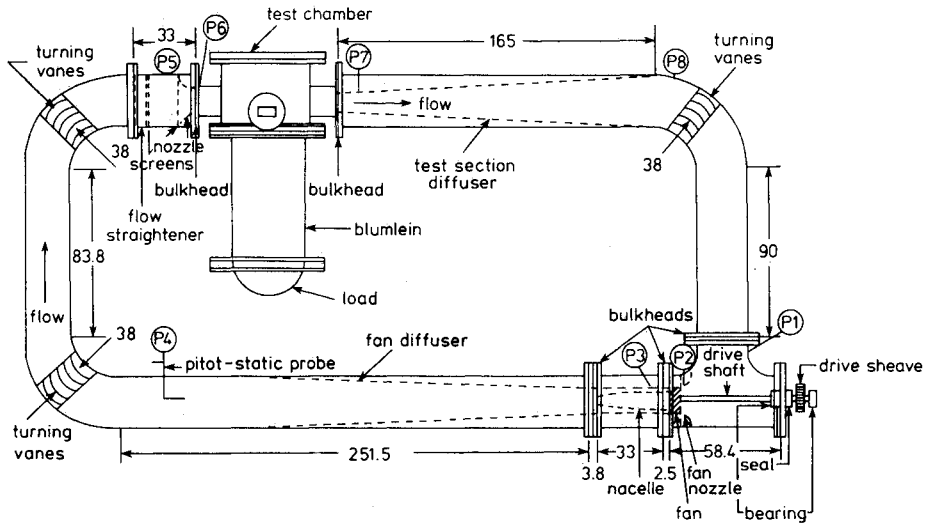

Fig. 2 Schematic of low-speed, high-pressure, closed-loop tunnel, showing pressure measurement locations; all dimensionless in cm.

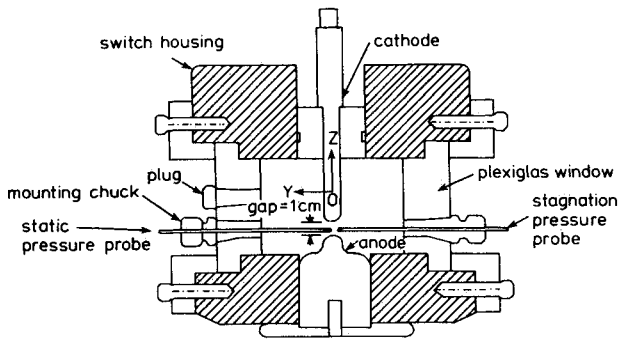

Fig. 3a Front view of spark gap switch housing with electrodes and flow diagnostic probes.

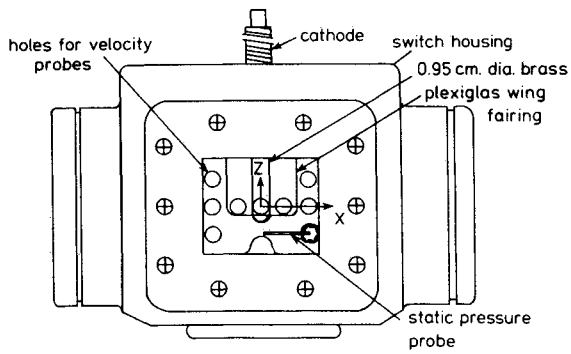

Fig. 3b Side view of spark gap switch housing with electrodes and flow diagnostic probes.

Other traverses at a gap spacing of $d = 0.56$ cm with $p = 1$ atm in air are shown in Fig. 5. The electrode geometry reduces the velocity by about 6% at $d = 0.87$ cm relative to test section velocities measured when no electrodes are installed; while at $d = 0.56$ cm, interelectrode velocity is reduced by 10% relative top clear tunnel velocity at the same tunnel drive fan speed.[4] These velocity reductions are due to the additional test section blockage (approximately 14%) due to the electrodes.

The mean velocity measured midway between the nipple-wing electrodes at a gap of 0.95 cm is shown vs tunnel drive fan speed in Fig. 6 for air and in Fig. 7 for a 10% mixture of SF_6 in N_2, for pressures between 170 and 722 kPa (10-90 psig). Mean velocity increases at the same fan speed as pressure is increased. Comparison of Figs. 6 and 7 indicates a similar effect as the gas density is increased. It is thought that this is due to a Reynolds number effect on either tunnel frictional loss coefficients or fan performance. Mean velocity is linear with fan speed, as expected. These interelectrode mean velocity results document the gas velocity for a wide range of conditions and, in conjunction with recovery results, enable spark gap performance parameters such as observed clearing factors to be calculated. Such considerations will be presented below.

A vertical pitot probe traverse between the electrodes on the tunnel centerline is shown in Fig. 8 for the first tunnel speed in air at $p = 1$ atm. Here a value of z equal to zero corresponds to the surface of the bottom nipple electrode. Again, the mean velocity profile is quite uniform away from either electrode surface, and low-frequency relative velocity fluctuations are on the order of 0.5%.

To document more completely the turbulence levels occurring in the interelectrode region and to permit studies of the

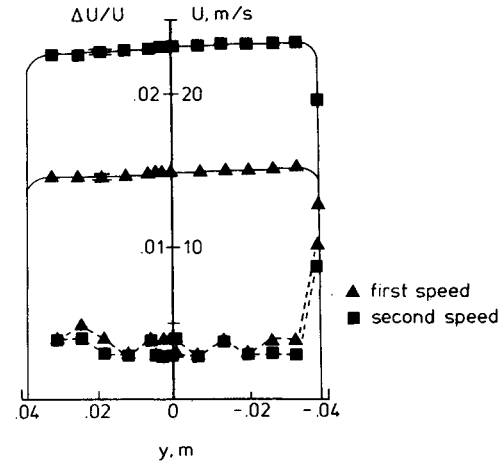

Fig. 4 Horizontal profiles of mean velocity and low-frequency relative velocity fluctuations midway between electrodes; nipple-wing electrodes in low-speed tunnel, $d=0.87$ cm, $p=1$ atm, 100% N_2.

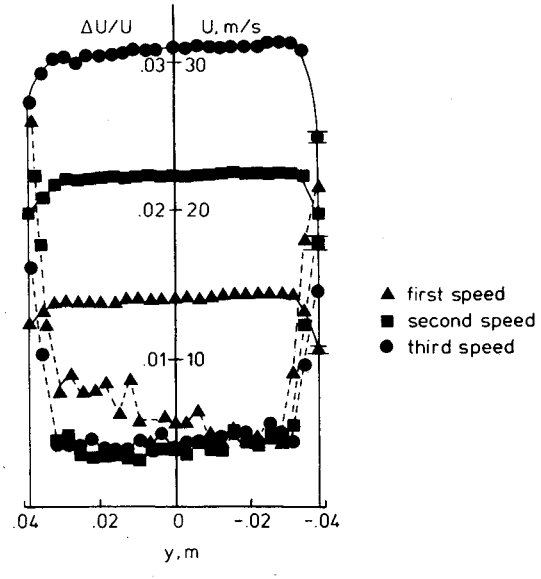

Fig. 5 Horizontal profiles of mean velocity and low-frequency relative velocity fluctuations midway between electrodes; nipple-wing electrodes in low-speed tunnel, $d=0.56$ cm, $p=1$ atm, air.

effect of freestream turbulence on gas-flow spark gap recovery, a series of mean and fluctuating velocity surveys has been conducted using both one- and two-sensor hot-wire anemometer probes. Profiles have been measured in the interelectrode region with various turbulence manipulator devices installed upstream of the low-speed tunnel test section nozzle. These turbulence manipulators have consisted either of honeycomb flow straighteners and fine mesh screens to reduce freestream turbulence or of coarse mesh grids consisting of plates drilled with circular holes in a regular, hexagonal pattern to generate turbulence. A two-channel anemometer operated in the constant temperature mode has been used. The linearized probe output has been calibrated against a pitot probe located 0.64 cm away from the hot wire. Turbulence intensity levels have been obtained from mean and rms voltages, where rms voltages have been measured using a true rms voltmeter.

Typical data obtained with no electrodes installed in the test section (clear tunnel) are shown in Figs. 9 and 10 at a pressure of 444 kPa (50 psig) in air at the second tunnel speed. Mean velocity increases somewhat near the right test section wall, but this may be due to increased blockage as the hot-wire probe was inserted into the test section through the right wall. This probe blocks about 7% of the cross-

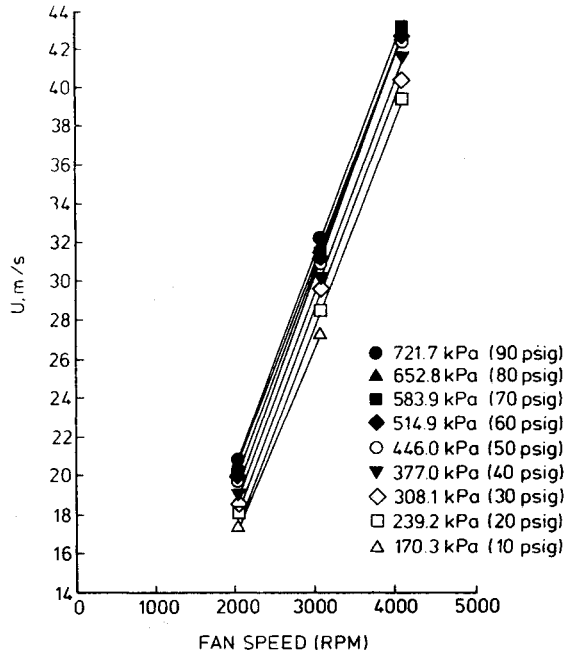

Fig. 6 Mean velocity between nipple-wing electrode pair in low-speed tunnel; $d=0.95$ cm; air.

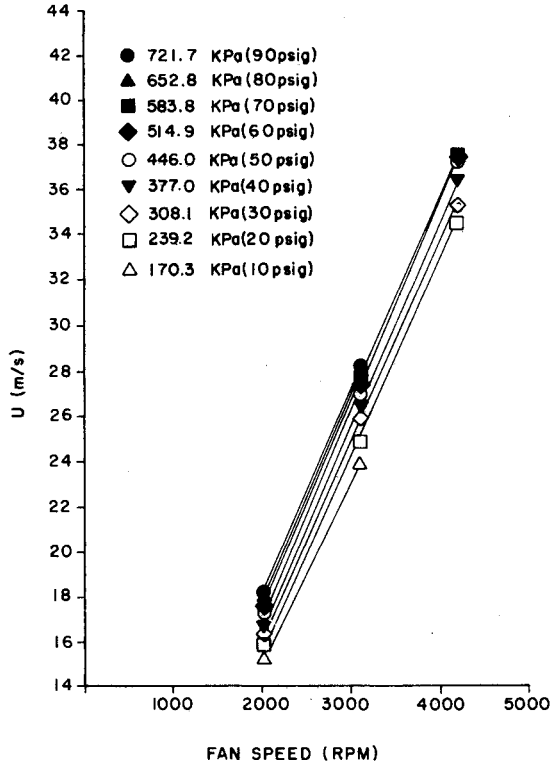

Fig. 7 Mean velocity between nipple-wing electrode pair in low-speed tunnel; $d=0.95$ cm; 10% SF_6-90% N_2.

sectional area of the test section when traversed to the left wall. The mean velocity is slightly less than that measured in an earlier experiment using a pitot probe (Fig. 6). The mean velocity is reduced 5.5-6.5% by the turbulence manipulators relative to cases in which no screens are installed. Longitudinal turbulence intensities are about 2.2% for the 2.54-cm-diam hole turbulence-generating plate, around 0.5-1.5% when no turbulence manipulators are installed, and 0.1 to 0.4% for the honeycomb and two screens. Similar turbulence intensity profiles are observed at other pressures and for the other tunnel speeds, but turbulence intensity tends to increase slightly at the

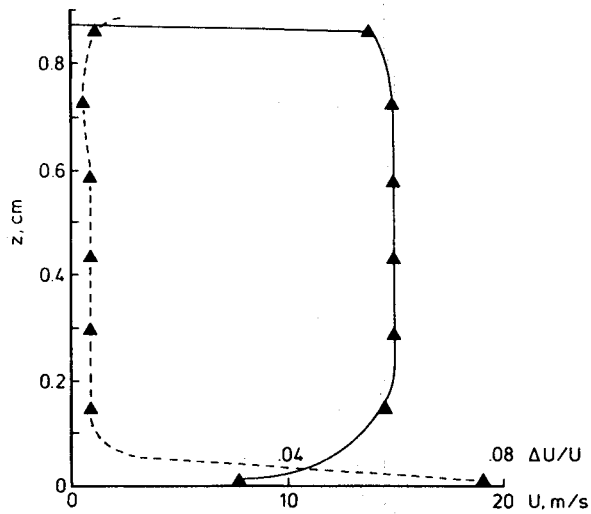

Fig. 8 Mean velocity and low-frequency relative velocity fluctuation profile on tunnel centerline; nipple-wing electrodes in low-speed tunnel, $d=0.87$ cm, $p=1$ atm, 100% N_2, first tunnel speed.

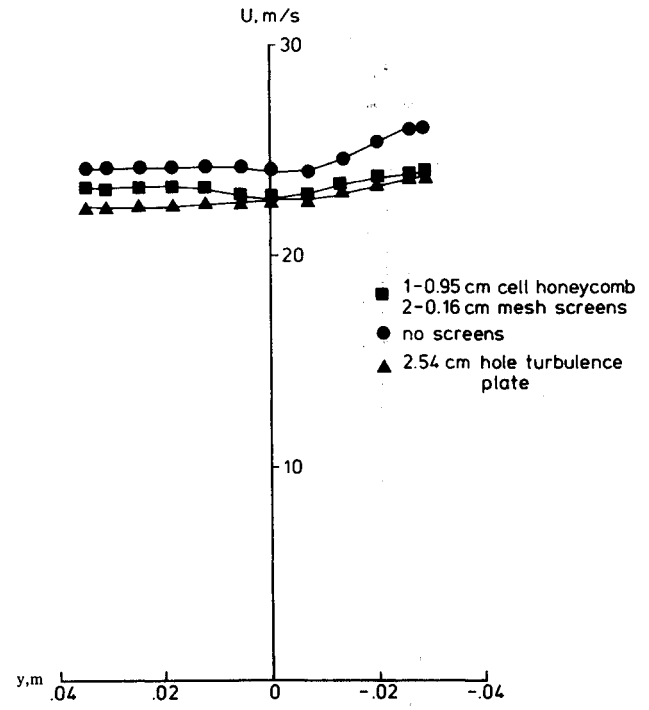

Fig. 9 Horizontal profiles of mean velocity in low-speed tunnel, $z=0$, $p=4444$ kPa (50 psig), air, second tunnel speed, empty test section.

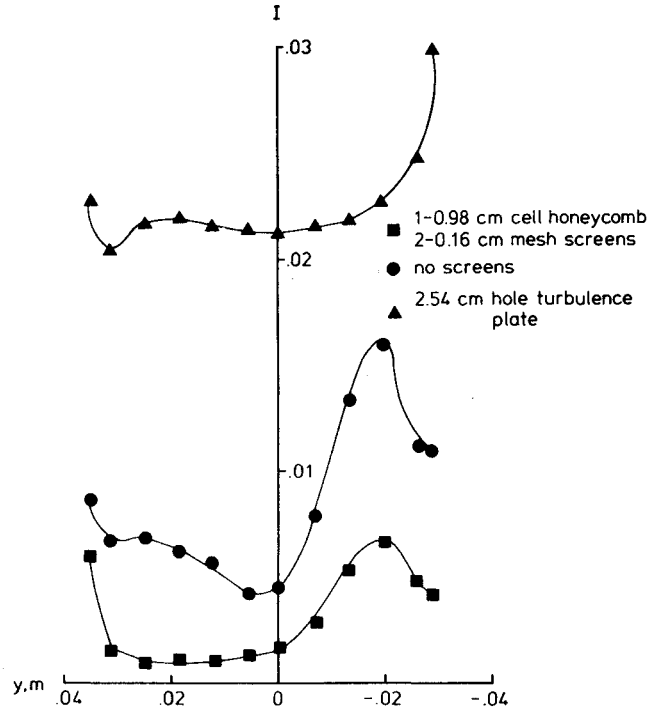

Fig. 10 Horizontal profiles of turbulence intensity in low-speed tunnel, $z=0$, $p=444$ kPa (50 psig), air, second tunnel speed, empty test section.

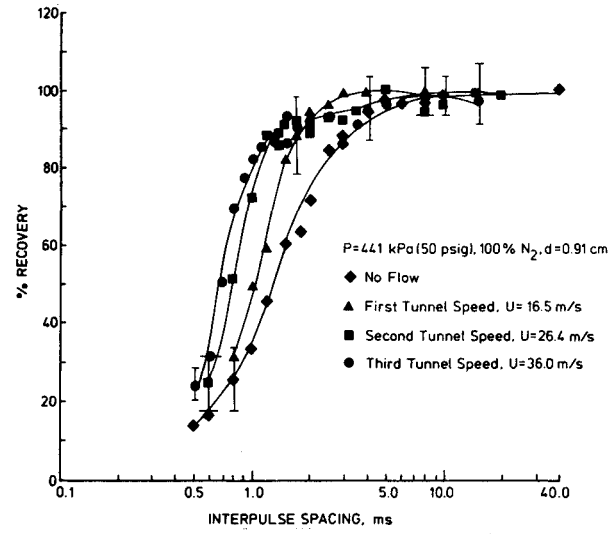

Fig. 11 Recovery data for nipple-wing electrode pair in low-speed tunnel; $d=0.91$ cm, $p=441$ kPa (50 psig), 100% N_2, $\bar{V}_1=97$ kV.

third tunnel speed. Turbulence levels also consistently increase toward the right test section wall. Other turbulence measurements not presented herein indicate turbulence intensities in the wakes downstream of electrodes to be much higher, on the order of 40%. Earlier velocity data were obtained with no turbulence manipulators installed (Figs. 4-8).

Electrical Recovery Results

Examples of typical electrical recovery performance are shown in the curves in Figs. 11 and 12 obtained for the nipple-wing electrode pair installed in the low-speed tunnel for an interelectrode gap of 0.91 cm for 100% N_2 at pressures of 441 and 714 kPa (50 and 90 psig). Recovery has been defined as the ratio of second- to first-pulse breakdown voltage for each two-pulse burst. Each data point in the figures corresponds to the average of 50 bursts at each interpulse spacing. Also shown in Figs. 11 and 12 are standard deviations representative of the statistical variation in recovery. These recovery results have been obtained with no turbulence manipulators installed. Comparison of Figs. 11 and 12 indicates that switch recovery improves somewhat with increasing pressure for 100% N_2, both with and without gas flow. Other data not presented indicate that SF_6 does not greatly influence switch recovery at $d=0.91$ cm although the first-pulse breakdown voltage is increased from 97 to 148 kV at a fixed gap spacing. Clearly the most significant reduction in switch recovery time is that due to gas flow where times for 70% recovery are reduced relative to no-flow recovery by factors of 2.3-2.4 at the maximum velocity of nominally 36-38 m/s. More impressive behavior has been observed at a gap of 0.53 cm (Fig. 13), where reductions in recovery time relative to the no-flow case by a factor of as much as 3.8 are observed at the smaller gap at a maximum interelectrode velocity of 36.2 m/s. However, it should be

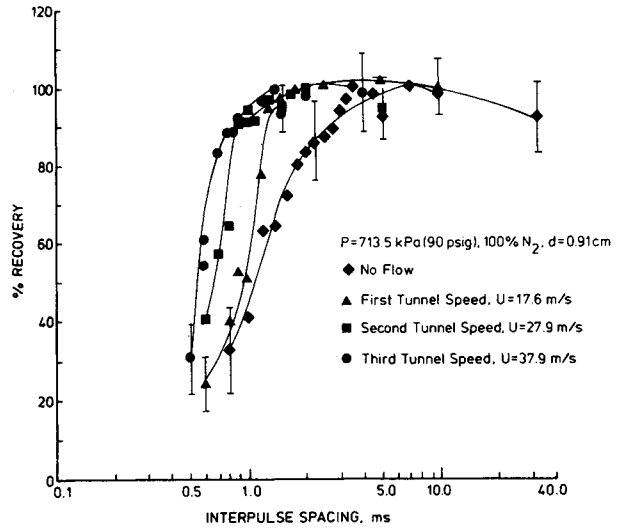

Fig. 12 Recovery data for nipple-wing electrode pair in low-speed tunnel; $d=0.91$ cm, $p=714$ kPa (90 psig), 100% N_2, $\bar{V}_1=125$ kV.

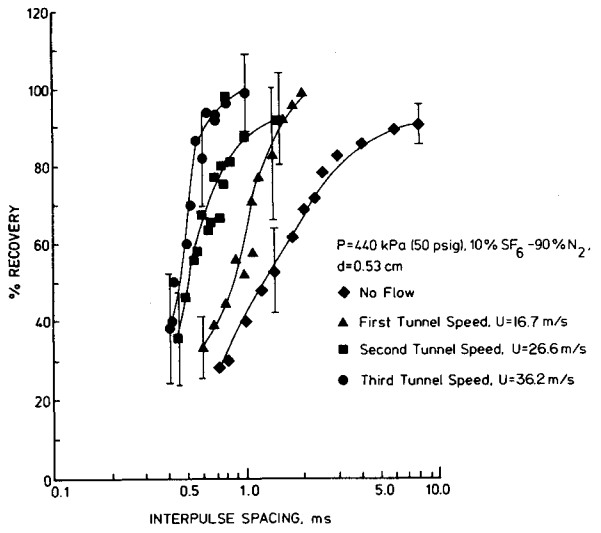

Fig. 13 Recovery data for nipple-wing electrode pair in low-speed tunnel; $d=0.53$ cm, $p=440$ kPa (50 psig), 10% SF_6-90% N_2, $\bar{V}_1=118$ kV.

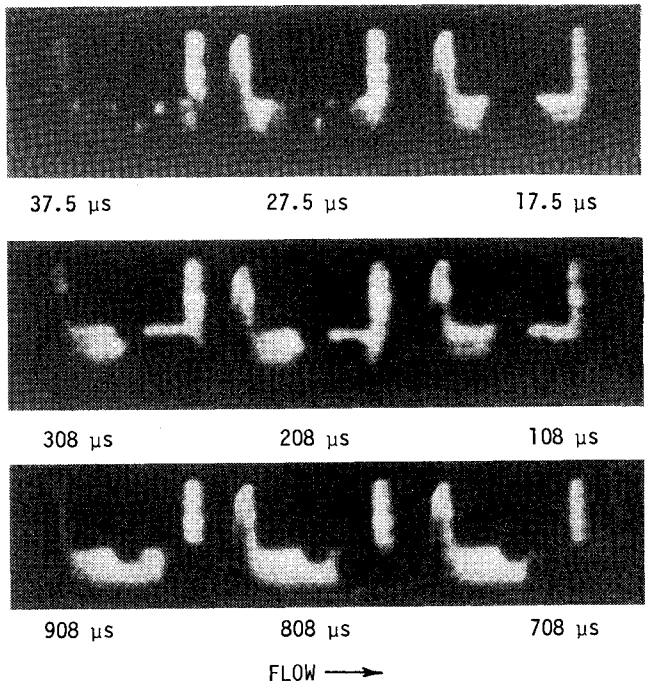

Fig. 14 Typical schlieren image converter camera photographs for nipple-wing electrodes installed in low-speed tunnel at $p=445$ kPa (50 psig) in 100% N_2 at $d=1.0$ cm, third tunnel speed.

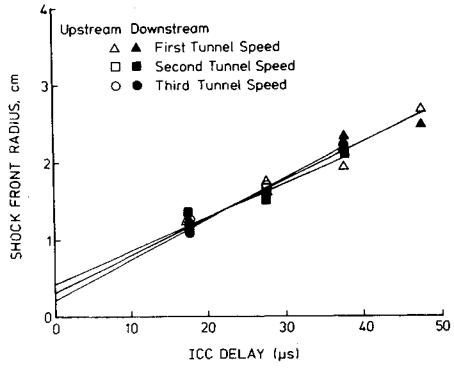

Fig. 15 Shock position vs time; nipple-wing electrodes in low-speed tunnel, $d=1.0$ cm, $p=446$ kPa (50 psig), 100% N_2.

mentioned that the long-term performance of this electrode geometry is degraded somewhat, apparently due to increased surface tracking, which occurs once arc products have been deposited on the Plexiglas wing just downstream of the top electrode.

Optical Flow Diagnostics

Examples of schlieren image converter camera photographs for the first arc disturbance between the nipple-wing electrode pair at 446 kPa (50 psig) in 100% N_2 at a gap spacing of $d=1.0$ cm are shown in Fig. 14 for the third tunnel speed (34.8 m/s). Photographs are presented for times after the first arc between 17.5 and 907.5 μs where the exposure time for these pictures was 5 μs. These data have been obtained with turbulence reduction honeycomb and screens installed in the tunnel. A comparison with similar photographs with no gas flow shows that the flow significantly alters the spreading and convection of the heated gas for times after the arc on the order of 100 to 200 μs or greater. The arc-generated shock is visible for times up to 47.5 μs after application of the voltage pulse. Expansion and mixing of the heated arc debris may be seen by comparing subsequent pictures. In a similar manner, convection of the arc debris with the mean flow may also be seen. Furthermore, it appears that heated gas from the arc moves away from the interelectrode region more slowly near the electrodes than in the mid-gap region. Similar trapping of heated gas from prior arcs in the lee of electrodes has been observed at lower voltages and velocities by Pederson et al.[6] It appears that such trapping of heated gas from prior arcs is one of the governing factors in determining the recovery time for this electrode geometry; in addition it also leads to increased surface tracking.

Measured shock radius vs time, from the schlieren flow diagnostic data, is presented in Fig. 15 for three tunnel speeds. For this electrode geometry at a gap spacing of $d=1.0$ cm, and 17.5 μs $\leq t \leq$ 47.5 μs, the shock radius is observed to increase nearly linearly with time. Linear curve fits to these data yield an average shock propagation speed of 470 m/s, corresponding to a Mach number of 1.37. However, it is noted that for $t<17.5$ μs, the shock speed was significantly higher. It is expected that dR/dt is not constant and must slow to acoustic speed at later times as the shock further weakens.

An example of the measured arc debris position vs time, from the schlieren optical flow diagnostic data, is presented in Fig. 16. Shown are the measured locations of the upstream edge of the heated arc debris, an approximate

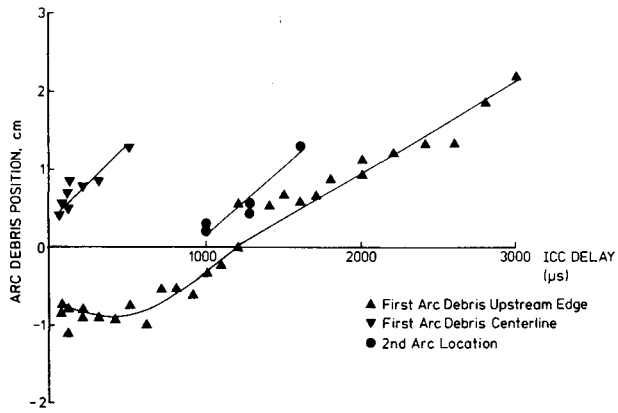

Fig. 16 Arc debris position vs time; nipple-wing electrodes in low-speed tunnel, $d = 1.00$ cm, $p = 446$ kPa (50 psig), 100% N_2, first tunnel speed.

center of the arc debris (obtained as the average of the positions of the upstream and downstream edges), and locations of second arcs for selected interpulse spacings between 1 and 1.6 ms. These data are plotted for the first tunnel speed (15.7 m/s). Measured positions are plotted vs elapsed time between application of the first voltage pulse to the switch and the middle of the 5-μs ICC exposure time. The upstream edge of the heated arc debris remains at a position of nominally 0.8 cm upstream of the electrode axis for times as great as 500 μs. Once the upstream edge of the arc debris begins to move in the downstream direction, this motion occurs at constant velocity. Also, motion of the arc debris center occurs at a constant velocity but at a higher velocity (steeper slope) than that observed for the debris upstream edge motion. Motion of the arc debris center is always in the downstream direction, and it appears that the arc originates approximately 0.4 cm downstream of the geometric electrode centerline, where the electrode radius is 0.48 cm. Similar behavior is observed at the other tunnel speeds, except that arc debris convection velocities increase as tunnel velocity is increased. Also, the time delay before the upstream edge of the heated arc debris is observed to move initially downstream decreases as tunnel velocity is increased. This time delay is less than 20 μs at the third tunnel speed, consistent with observations of Pederson et al.[7] that spark gap recovery was not greatly improved by gas flow below a critical velocity value. Second arc location for c-shaped arcs is observed to be near the upstream edge of the prior arc debris. Similar phenomena have been observed at lower voltages (11-15 kV) and higher velocities (180-360 m/s) by Molen et al.[8]

These results are summarized in Table 1, where pitot probe velocity measurements midway between the electrode at all three tunnel speeds are compared with velocities from least-square-curve fits to the linear portions of the arc debris position vs time data. Also shown are measured arc debris spreading velocities. It is observed that the heated arc debris center moves at a velocity very close to the measured gas velocity while the upstream edge of the arc debris moves more slowly. This is explained by the fact that at the same time the heated gas is convecting in the mean flow direction, this heated gas region is growing in size due to turbulent diffusion as well as expansion for the smaller times. The observed arc debris spreading velocity is nearly constant, equal to about 17 m/s.

These results indicate that the time history of the heated arc debris for a gas-flow spark gap might be identical to the arc debris turbulent mixing and subsequent cooling that occurs in a spark gap with no flow,[9] with the exception of the debris being convected away from the interelectrode region by the gas-flow velocity. Thus, there are two different physical phenomena, each influencing recovery of a gas-flow

Table 1 Calculated arc debris convection and spreading velocities for nipple-wing electrodes in low-speed tunnel; $p = 446$ kPa (50 psig), 100% N_2, $d = 1.0$ cm

Tunnel velocity, m/s	Convection velocities, m/s: Debris center	Convection velocities, m/s: Debris upstream edge	Spreading velocity, m/s: Debris radius
15.7	17.5	11.6	16.5
24.9	24.5	17.1	17.5
34.8	29.3	21.3	16.8

spark gap in its own characteristic time scale: first, gas density increase due to cooling of the heated arc debris by turbulent diffusion and, second, convection of the heated arc debris away from the interelectrode region. Recently, results of a similar analysis of schlieren photographs of the interelectrode region for a second electrode geometry were presented, which support these conclusions.[10]

Clearing Factor

One simple measure of the performance of a gas-flow spark gap is the clearing factor, which may be defined as a ratio of a characteristic electrical recovery time divided by a characteristic flow time scale. If the recovery time without gas flow is long compared with the flow time scale, then it would be expected that the dominant means of achieving switch recovery would be removal of prior arc products from the electrode region. In this limit, then, clearing factor would be expected to be constant for a given electrode configuration, gas species, and pressure. This would lead to a linear model, where repetition rate would scale directly with gas velocity. However, there appears to be no means of relating the numerical value of such a clearing factor to physical mechanisms such as turbulent diffusion rates, or the presence of separated wakes, which certainly must influence switch recovery. Hence, clearing factor is at best a limited concept, useful in correlating and comparing experimental results.

Examples of calculated clearing factor values for the nipple-wing electrodes in the low-speed tunnel are shown in Fig. 17 at a gas pressure of 444 kPa (50 psig) in 100% N_2. Two sets of recovery experiments corresponding to two gap spacings ($d = 0.9$ cm and 0.53 cm) have been considered. Recovery times for 70% switch recovery have been normalized by a characteristic flow time to move one electrode radius R/U. The time for 70% switch recovery has been chosen to eliminate scatter in clearing factor due to a plateau in recovery observed at some lower pressures. These recovery results lead to clearing factors ranging from $3 \le CF \le 6$. It is noted that clearing factor tends to increase as d increases. Also, clearing factor is nearly constant with velocity in this velocity range. Slight increases in CF with increasing velocity are attributable to the decreased density for shorter elapsed time. Similar calculations for other electrode geometries indicate that CF changes most dramatically with electrode geometry, apparently increasing with increases in the effects of flow separation or surface tracking on downstream insulators.

Recovery Model

Analysis of the above clearing factor calculations and optical flow diagnostic results has led to the development of a simplified recovery model in which switch recovery is said to occur when the line integral of the density along all paths from one electrode to the other is greater than the fully recovered first-pulse breakdown value of ρd. That is, recovery with gas flow occurs when

$$\int_1^2 \rho(s)\,ds \ge \rho_\infty d \qquad (1)$$

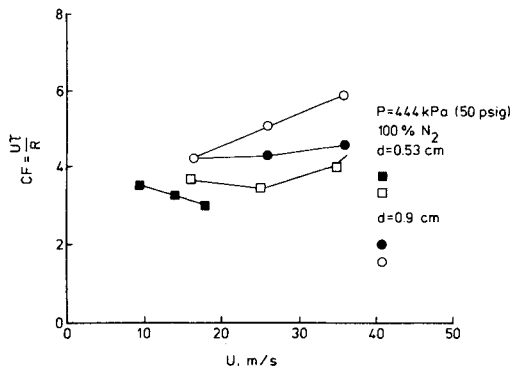

Fig. 17 Clearing factor based on electrode radius *CF* for 70% recovery, vs interelectrode velocity; nipple-wing electrode pair in low-speed tunnel, $p = 444$ kPa (50 psig), 100% N_2.

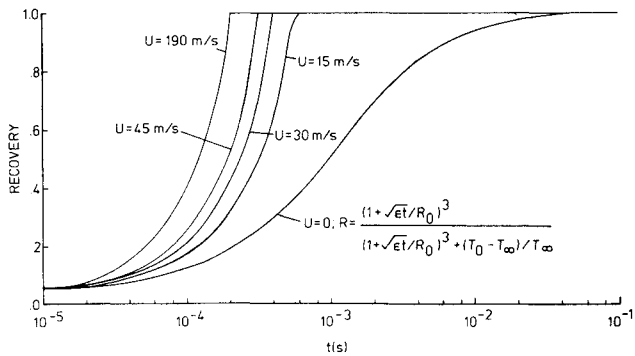

Fig. 18 Predicted spark gap recovery curves for simple recovery model, Eq. (2), assuming $d = 1.0$ cm, $T_0 = 10^4$ K, $T_\infty = 300$ K, $R_0 = 2$ mm, $\epsilon = 2 \times 10^{-3}$ m^2/s, for various interelectrode velocities.

for all possible paths from one electrode to the second. This concept was originally suggested less rigorously by Moran.[11] A great simplification that yields qualitatively correct recovery results is to separate the line integral into the product of an effective average density times an arc path length. This effective density is taken as the gas density for heated arc debris developed without including the effects of mean gas flow, while the arc path length for c-shaped arcs through prior heated arc debris is approximated by $(d + 2Ut)$. Thus, the recovery, when arcing through downstream prior arc debris may occur, would be given approximately by

$$R(t) = \frac{\rho(t)}{\rho_\infty} \cdot \frac{d + 2Ut}{d} \tag{2}$$

Once this recovery factor reaches 1, arc location should return along the electrode axis. Predicted recovery curves for no gas flow and for $U = 15$, 30, 45, and 190 m/s are shown in Fig. 18 for this model, where the simple no-flow density model adopted is obtained by assuming that the debris radius should increase with the square root of a constant turbulent diffusion coefficient $\times$ time. This leads to temperature decreasing with time proportional to $(t)^{-3/2}$, as with a point heat source.[12] For this simplified model,

$$\frac{\rho(t)}{\rho_\infty} = \frac{(1 + \sqrt{\epsilon t}/R_0)^3}{(1 + \sqrt{\epsilon t}/R_0)^3 + (T_0 - T_\infty)/T_\infty} \tag{3}$$

where R_0 and T_0 are the estimated initial radius and temperature of the arc debris, and ϵ is the turbulent diffusion coefficient. For curves shown in Fig. 18, it was assumed that: $R_0 = 2$ mm, $T_0 = 10^4$ K, $T_\infty = 300$ K, $d = 1$ cm, $\epsilon = 2 \times 10^{-3}$ m^2/s. This assumed model predicts the arc debris radius to grow as $\sqrt{t}$, which differs from experimental observation (Table 1). Also, the no-flow recovery curve (Fig. 18) is not as steep as experimental results (Figs. 11-13). This indicates that the turbulent diffusion coefficient is not a constant, as has been assumed in the model. However, even with these limitations, it is felt that the simple model shown in Fig. 18 helps to relate physical phenomena to recovery, and this model may be refined in the future to allow quantitative recovery predictions. The model also predicts a time when second arcs should return to the first arc location. However, the model in its present form does not include the effects of flow separation or surface tracking and has oversimplified the problem by assuming the arc debris density to be a constant. Further, there is a great deal of uncertainty as to the appropriate form of the turbulent diffusion coefficient, where this diffusion coefficient is expected to increase with time.

Conclusion

A series of experimental measurements of the performance of a gas-flow spark gap has been described. Physical gas-flow phenomena have been documented by pitot probe and hot-wire measurements, along with schlieren optical diagnostics. Performance of the spark gap has been characterized by a series of switch recovery curves at several gas velocities for various gas species, pressures, and gap spacing.

The mean velocity profiles in the interelectrode region have been found to be quite uniform. Interelectrode velocity increases at a constant tunnel drive fan speed in the low-speed tunnel as the gas density is increased, due to a Reynolds number effect. Interelectrode velocity also varies as the electrode geometry or gap spacing is changed, generally decreasing somewhat as the electrodes block a greater portion of the tunnel test section. Freestream turbulence levels were measured to be 0.5-1% when no screens were installed in the tunnel. Screens reduced test section turbulence intensity to 0.1-0.2%, while a turbulence generator resulted in a turbulence level of 2.2%.

Spark gap recovery times were found to be dramatically reduced with increasing gas velocity, relative to recovery times without gas flow. These recovery curves also were observed to steepen with the addition of gas flow. Observed recovery times and gas velocities were used to calculate clearing factors, which varied by a factor of 2 as gas velocity varied from 10 to 40 m/s, and as gap spacing varied by a factor of 2 for the nipple-wing electrode geometry. Clearing factor increases somewhat as gap spacing increases, but it increases only slightly with velocity (due to the decreased density recovery). The largest observed variations in clearing factor have been for changes in electrode geometry, where clearing factor, and hence recovery time, increased as the effects of flow separation and surface tracking increased.

Optical schlieren flow diagnostic data showed arc-generated shocks that propagated at a slightly supersonic Mach number, and indicated that the heated arc debris convects with the mean flow, while spreading, largely due to turbulent mixing.

These experimental results led to the formulation of a simplified gas-flow spark gap recovery model that appears to hold promise for predicting the effects of gas flow on recovery.

Acknowledgments

The authors acknowledge the efforts of colleague Hugh C. Kirbie and students David M. Barrett, Edward G. Ruf, and Sang Nam in this work. This work was supported by the Naval Surface Weapons Center under Contract N60921-81-C-A221.

References

[1]Kuhlman, J. M., "Survey of Gas Flow and Heat Transfer Effects on Performance of Gas Spark Gaps," *Workshop Proceedings,* DoD Workshop on Repetitive, High Power, Gas Spark Gaps, Durango, CO, Jan. 1983, pp. 85-153.

[2]Molen, G. M. and Carper, H. J., "Thermal and Gas Dynamic Effects," *Workshop Proceedings*, DoD Workshop on Repetitive, High-Power, Gas Spark Gaps, Durango, CO, Jan. 1983, pp. 217-262.

[3]Barrett, D. M., Kirbie, H. C., and Molen, G. M., "A 250-kV, 10-kHz, Two-Pulse Modulator," *Proceedings of the IEEE 4th Pulsed Power Conference*, June 1983, pp. 255-258.

[4]Ruf, E. G. and Kuhlman, J. M., "Low Speed Closed Circuit High Pressure Tunnel for Gas Flow Spark Gap Studies," AIAA Paper 84-1596, June 1984.

[5]Syvertson, C. A. and Savin, R. C., "The Design of Variable Mach Number Supersonic Nozzles by Two Procedures Employing Inclined and Curved Sonic Lines," NACA TN 2922, March 1953.

[6]Pederson, R. J. and Carper, H. J., "Flow Visualization in a Gas Blown Spark Gap," *Proceedings of the IEEE 15th Pulsed Power Modulator Symposium*, IEEE Publication 82CH 1785-5, June 1982, pp. 107-109.

[7]Pederson, R. J., Borger, M. A., and Carper, H. J., "Effects of Flow Velocity and Electrode Divergence Angle on the Performance of a Repetitively Pulsed, Gas-Blown Spark Gap Switch," *Proceedings of the 16th Power Modulator Symposium*, IEEE Publication 84CH 2056-0, June 1984, pp. 48-53.

[8]Molen, G. M., Ruf, E. G., Kuhlman, J. M., and Bernardes, J. S., "Gas-Flow Switch Recovery Experiments," *Proceedings of the IEEE 4th Pulsed Power Conference*, Albuquerque, NM, June 1983, pp. 166-169.

[9]Bel'kov, E. P., "Gas Cooling and Electric Strength Recovery After a Spark Discharge," *Soviet Physics—Technical Physics*, Vol. 16, No. 8, Feb. 1972, pp. 1321-1323.

[10]Kuhlman, J. M., Molen, G. M., Srinivasan, S., Nam, S. H., and Tiwari, S. N., "Arc-Generated Flow Phenomena in High-Power Repetitively-Pulsed Gas-Flow Spark Gaps," *Proceedings of the IEEE 5th Pulsed Power Conference,* Arlington, VA, June 1985, to be published.

[11]Moran, S. L., personal communication, 1984.

[12]Carslaw, H. S. and Jaeger, J. C., *Conduction of Heat in Solids*, Oxford University Press, New York, 1959, Chap. 10.